



An artificial organic-inorganic Z-scheme photocatalyst $\text{WO}_3@\text{Cu@PDI}$ supramolecular with excellent visible light absorption and photocatalytic activity



Wengao Zeng^{a,b}, Tao Cai^{a,b}, Yutang Liu^{a,b,*}, Longlu Wang^c, Wanyue Dong^{a,b}, Hui Chen^{a,b}, Xinnian Xia^d

^a College of Environmental Science and Engineering, Hunan University, Lushan South Road, Yuelu District, Changsha 410082, PR China

^b Key Laboratory of Environmental Biology and Pollution Control (Hunan University), Ministry of Education, Lushan South Road, Yuelu District, Changsha 410082, PR China

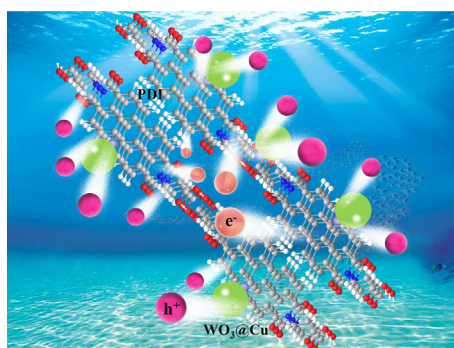
^c School of Physics and Electronics, Hunan University, Changsha 410082, PR China

^d College of Chemistry and Chemical Engineering, Hunan University, Changsha 410082, PR China

HIGHLIGHTS

- Organic-inorganic $\text{WO}_3@\text{Cu@PDI}$ heterostructure was prepared.
- Z-scheme heterostructure promote charge transport and separation.
- 30% $\text{WO}_3@\text{Cu@PDI}$ heterostructure possesses highest degradation rate.
- Z-scheme mechanism was demonstrated by ESR and experimental observations.

GRAPHICAL ABSTRACT



ARTICLE INFO

Keywords:

WO_3
PDI
Z-scheme
Photocatalytic degradation

ABSTRACT

Tungsten trioxide (WO_3) has a wide application in environmental remediation due to its stability. Yet, the application of WO_3 is severely limited by its wide band gap and weak electron reduction ability. In this work, we intend to enhance the visible light absorption and photocatalytic performance by constructing an organic-inorganic Z-scheme system $\text{WO}_3@\text{Cu@PDI}$. Apparently, $\text{WO}_3@\text{Cu@PDI}$ has excellent visible light absorption and photocatalytic degradation ability in the degradation of tetracycline hydrochloride (TC). Under visible light irradiation, the degradation rate of composites is 40 times faster than that of sole WO_3 and 5 times than PDI. The photocatalytic activity of $\text{WO}_3@\text{Cu@PDI}$ toward TC still kept 85% after three reuses. We revealed that this high photoactivity arisen from the efficient carriers separation and the formation of Z-scheme junction. Importantly, this Z-scheme electron transfer pathway was confirmed by thorough experimental study. This work demonstrated the significant potential of WO_3 -based inorganic-organic Z-scheme photocatalyst in environmental remediation.

* Corresponding author at: College of Environmental Science and Engineering, Hunan University, Lushan South Road, Yuelu District, Changsha 410082, PR China.
E-mail address: yt_liu@hnu.edu.cn (Y. Liu).

1. Introduction

Under the pressure of environment and energy, photocatalysis has become the focus of our attention as a means of green potential [1]. However, due to the low conversion efficiency of sole photocatalyst for solar energy, there are enormous challenges in the practical application [2,3]. Therefore, scientists tend to develop semiconductor catalysts with higher photocatalytic activity. Tungsten trioxide (WO_3) is widely used in photocatalytic degradation and hydrogen production due to its very positive valence band ($\text{VB} = 3.44 \text{ eV VS NHE}$) [3,4]. But the wide band gap and weak electron reduction ability of WO_3 still limit its practical application [5,6]. Therefore, for the practical application of WO_3 , the key is how to increase its visible light absorption capacity and separation of electron-hole pairs.

In the process of photocatalytic degradation, photocatalysts must have a suitable band gap and effective carrier separation in order to have a strongly photocatalytic ability [7–9]. The wide band gap and weak electron reduction ability of WO_3 greatly limit his practical application. In order to improve the photocatalytic activity and visible light absorption of WO_3 , many WO_3 -based composites have been studied in the past, such as WO_3/CuO [10], $\text{WO}_3/\text{BiVO}_4$ [11], $\text{BiVO}_4/\text{WO}_3/\text{SnO}_2$ [12]. These methods have proved the improvement of WO_3 performance by accelerating electron transfer. However, these methods can't absolutely solve the practical application problems of WO_3 . The formation of a heterojunction accelerates the transmission of electrons but does not retain redox ability.

As we know, the advantage of the Z-scheme is that photon-generated electrons and photon-generated holes produced in two different components can be directly combined [13–15], which can well retain the redox ability of WO_3 . But at present, most of them use noble metals as electron transfer media and inorganic semiconductors as electron acceptors, such as $\text{Ag}/\text{WO}_3/\text{Bi}_2\text{WO}_6$ [16], $\text{Ag}_2\text{CO}_3/\text{Ag}/\text{WO}_3$ [17]. It is well known that the large-scale application of photocatalyst in photocatalysis not only depends on its higher catalytic activity, but also takes into account its price and environmental friendliness. Therefore, the replacement of precious metals with non-noble metal (such as Cu [18,19]) reduces the cost while retaining good electronic transmission capacity. Additionally, compared with inorganic semiconductors, organic semiconductor materials are more attractive than inorganic material due to their tenability, optical performance, easy modification, structural variety, low cost and abundant elements [20,21]. Very recent, Zhu et al reported a typical n-type organic semiconductor perylene diimide (PDI). Extremely narrow band gap and suitable conduction band of PDI can effectively enhance the visible light absorption and photocatalytic activity of the composite [22]. Thus, the design of $\text{WO}_3@\text{Cu}@PDI$ Z-scheme system is very necessary. However, to the best of our knowledge, no one has done this work yet.

Herein, we synthesized the Z-scheme system of $\text{WO}_3@\text{Cu}@PDI$ (Scheme 1). We evaluated the activity of photocatalyst by degrading tetracycline (TC), which is widely present in our daily lives and harmful to our health. Taking more than 2 g per day can cause liver toxicity. The experimental results demonstrated the superior photocatalytic activity of $\text{WO}_3@\text{Cu}@PDI$. At the same time, the experiment was carried out in a TC solution containing various inorganic salts (K^+ , Na^+ , NO_3^- , Cl^-) to illustrate the practical application possibilities of the materials. Here, we also have demonstrated the flow of electrons in the composite and a simple degradation mechanism for tetracycline hydrochloride through sacrificial experiments and electron spin resonance (ESR) measurements. We have proved that it is a Z-scheme system with superior photocatalytic properties.

2. Experimental

2.1. Chemicals

Nanometer tungsten trioxide (WO_3 , < 100 nm, 99.9% metal basis)

were purchased from MACKLIN. Perylene-3,4,9,10-tetracarboxylic dianhydride ($\text{C}_{24}\text{H}_8\text{O}_6$, 98%), imidazole ($\text{C}_3\text{H}_4\text{N}_2$, 99%) and β -Alanine ($\text{C}_3\text{H}_7\text{NO}_2$, 99%) were purchased from Aladdin. Triethylamine ($\text{C}_6\text{H}_{15}\text{N}$, $\geq 99\%$), Copper(II) nitrate trihydrate ($\text{Cu}(\text{NO}_3)_2 \cdot 3\text{H}_2\text{O}$) and other reagents were purchased from Sinopharm Chemical Reagent Co. Ltd. All chemicals used were analytic grade reagents without further purification.

2.2. Preparation of PDI

The synthesis of PDI was a typical method according to Zhu's article [23]. 1.376 g of Perylene-3,4,9,10-tetracarboxylic dianhydride, 2.5 g of β -Alanine and 18 g of imidazole were placed in a 500 mL three-necked flask. Under the protection of argon, the flask was heated at 100°C for four hours. After cooled to room temperature, 100 mL ethanol and 300 mL hydrochloric acid (2 M) were added and stirred overnight. The final red solid was collected by filtration through a $0.25 \mu\text{m}$ membrane and washed with deionized water until the pH of the filtrate was neutral. Finally, the solid was dried at 60°C in oven.

2.3. Preparation of $\text{WO}_3@\text{Cu}$

Copper was deposited on WO_3 by a relatively simple and easy-to-operate photo-deposition method based on our team's previous work [24]. 300 mg of WO_3 was dissolved in ethanol solution ($V_0/V = 15\%$), after 30 min of ultrasound, 10 mL copper(II) nitrate trihydrate solution (containing 120 mg copper nitrate trihydrate) was added in the above solution ($\text{Cu}:\text{WO}_3 = 1:10$). Then it was irradiated with a 300 W Xe lamp (ultraviolet light) for 90 min in the case of N_2 circulation. The obtained $\text{WO}_3@\text{Cu}$ solution was used for subsequent use.

2.4. Preparation of Self-assembled PDI supermolecule

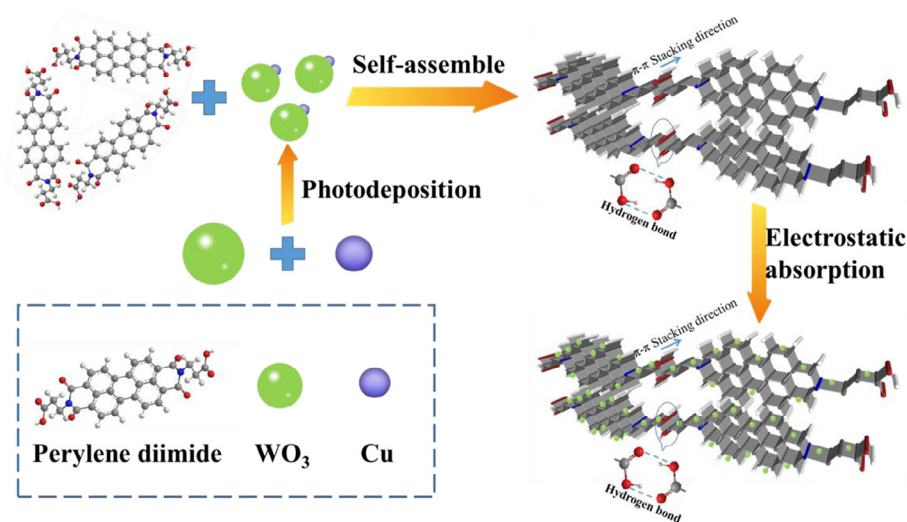
200.0 mL PDI (*N,N'*-bis(propionic acid)-phenyl-3,4,9,10-tetracarboxylic acid diimide) solution was added 834 μL triethylamine solution. After the solution turned red completely, 27.3 mL 4.0 M HCl was added in it to form PDI supermolecule. The final product was washed several times with deionized water. Finally, the solid was dried at 60°C in oven.

2.5. Synthesis of $\text{WO}_3@\text{Cu}@PDI$ composites

200.0 mL PDI (*N,N'*-bis(propionic acid)-phenyl-3,4,9,10-tetracarboxylic acid diimide) solution was added 834 μL triethylamine solution. Three 187.27 mL solutions (PDI 500 mg) were taken, and 125 mg, 214.3 mg, and 333.3 mg of $\text{WO}_3@\text{Cu}$ were separately added thereto, and continuously stirred for a while to form a composite material. According to the proportion of $\text{WO}_3@\text{Cu}$ in composite materials, composite material is named 20% $\text{WO}_3@\text{Cu}@PDI$, 30% $\text{WO}_3@\text{Cu}@PDI$ and 40% $\text{WO}_3@\text{Cu}@PDI$ respectively. Then we added 25.56 mL 4.0 M HCl to the solution and heated it for a hour in a water bath at 60°C . The product was washed to neutral by centrifugal separation and dried at 60°C [25].

2.6. Characterization

X-ray diffraction (XRD) with Cu-K α radiation (Rigaku, Smartlab) and X-ray photo-electron spectroscopy (XPS) with Al-K α radiation (Thermo Fisher Scientific, England) were used to detect the crystal structure and chemical composition of materials. The field emission scanning electron microscopy (FE-SEM) (Hitachi, S-4800) and transmittance electron microscopy (TEM) (JEOL, JEM-2100F) were used to determine the morphological characteristics of materials (as-prepared materials were loaded with molybdenum mesh). UV-vis diffuse-reflectance was recorded by an UV-vis spectrophotometer (Cary 300, Varian) with a measurement range of 200–800 nm. The



Scheme 1. Schematic representation of $\text{WO}_3@Cu@PDI$ composite synthesis.

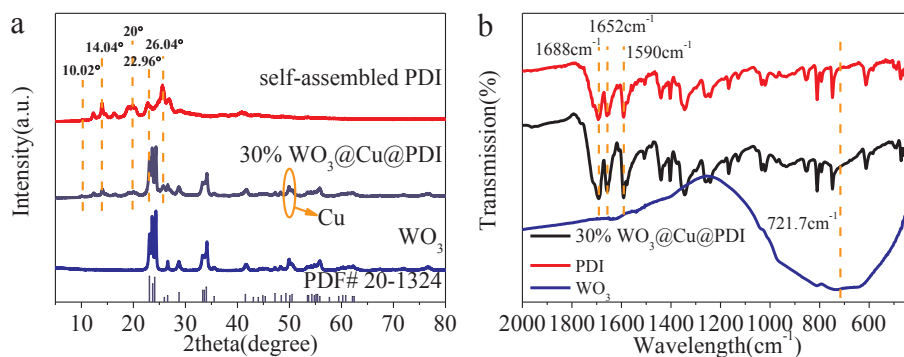


Fig. 1. (a) XRD pattern of samples. (b) FTIR spectra of samples.

photoluminescence (PL) spectra of PDI supermolecule and composites (at excitation wavelength of 468 nm) were measured by Hitachi F-7000 fluorescence spectrophotometer [25]. Electron spin resonance of material was detected by JES FA200 electron paramagnetic resonance spectrometer.

2.7. Evaluation and measurement of photocatalytic degradation performance

Degradation of pollutant was achieved under a 300 W Xe lamp with a cut off filter ($\lambda > 420$ nm) irradiation, which the irradiance was about 750 W/m^2 . Typically, 5 mg of as-prepared catalyst was added to TC contaminant solution (50 mL, 20 mg/L). Before irradiation, the suspension was ultrasonic for 10 min and stirred for half an hour to reach an adsorption-desorption equilibrium. Then 2 mL suspension was taken out every three minutes. The concentration of reactant was analyzed by UV-vis spectrophotometer.

2.8. Electrochemical measurement

Photocurrent response of the pre-prepared catalysts was measured under open circuit voltage. Electrochemical impedance spectroscopy of the pre-prepared catalysts was measured in frequency range of 0.01–10,000 Hz and open circuit voltage. Mott-Schottky of WO_3 was measured at the initial potential of 0 V and the termination potential of 1 V, while the PDI supermolecule was measured at the range of -0.5 to 0.5 V. The electrochemical workstation (CHI 660C) used for measurement was a standard three-electrode electrochemical system. Working electrode was the ITO deposited with catalysts, reference electrode was

Ag/AgCl chloride electrodes and counter electrode was a platinum wire. Na_2SO_4 (0.1 M) was used as an electrolyte solution in the working process. ITO deposited with pre-prepared catalysts was prepared by dip-coating method. Firstly, the 5 mg of $\text{WO}_3@Cu@PDI$ was placed in 0.75 mL ethanol solution. The suspension was ultrasonically dispersed for a certain period of time. Then the slurry was evenly coated on a indium-tin oxide (ITO, $2 \text{ cm} \times 4 \text{ cm}$). Finally ITO was dried at 60°C in the oven.

3. Results and discussion

3.1. Characterizations of materials

The crystal structures of pre-prepared WO_3 , self-assembled PDI supermolecule and 30% $\text{WO}_3@Cu@PDI$ (WO_3 loading has been optimized) were identified by X-ray diffraction. As can be seen from Fig. 1a, some similar peak at $2\theta = 10.02^\circ, 14.04^\circ, 20^\circ, 22.96^\circ, 26.04^\circ$ can be detected in PDI and $\text{WO}_3@Cu@PDI$ [23,25], which indicates WO_3 integrated into PDI supermolecule without changing PDI crystal structure. Similarly, some similar peak at $2\theta = 23.082^\circ, 23.707^\circ, 24.098^\circ, 34.021^\circ, 49.325^\circ, 50.493^\circ$ can be detected in WO_3 and $\text{WO}_3@Cu@PDI$. It is worth noting that the peak strength of the composite is lower than sole material. In addition, it can also be noted from Fig. 1a that the weak peak signal of copper is present, which indicates that copper is evenly dispersed in composite materials. These phenomena indicate that $\text{WO}_3@Cu@PDI$ was successfully synthesized. It can be seen from the FTIR spectrum of Fig. 1b that that the peak of WO_3 is mainly absorbed at $400\text{--}1200 \text{ cm}^{-1}$ (O-W-O). Similarly, as can be seen from Fig. 1b, the peaks of PDI supermolecule are mainly absorbed at

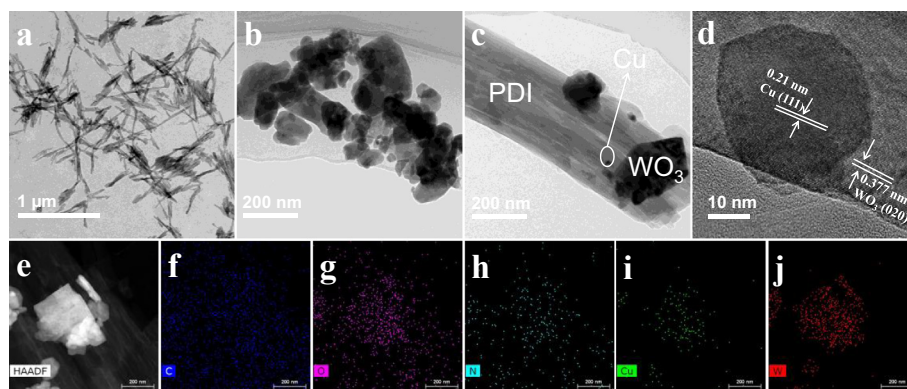


Fig. 2. TEM images of (a) self-assembled PDI, (b) WO₃, and (c) WO₃@Cu@PDI composite. (d) HRTEM image of WO₃@Cu@PDI composite, (e–j) C, O, N, Cu, W element mapping of WO₃@Cu@PDI composite.

1688 cm⁻¹ (C=O) and 1652 cm⁻¹ (C=C), indicating the carboxyl and benzene ring structures of PDI supermolecule. Additionally, the FTIR spectrum of WO₃@Cu@PDI contains all the peak signals of PDI and WO₃, which indicating that WO₃@Cu@PDI was successfully synthesized. And the synthesis of WO₃@Cu@PDI does not affect the chemical structure of WO₃ and PDI supermolecule.

(HR)TEM and SEM were used to investigate the morphologies of materials. SEM of Fig. S1(a, b) show that self-assembled PDI supermolecule is a clustered nanorod-like morphology and WO₃ is a lumpy structure. As shown in Fig. S1c, WO₃@Cu clearly sticks to PDI supermolecule. In order to further analyze the internal structure of the material, the (HR) TEM images are given in Fig. 2. Fig. 2a and b show that PDI is a nanorod with a diameter of 50 nm, WO₃ is a nanoparticle with a size of 50–100 nm and the average size of Cu NPs is 4 nm, respectively. From Fig. 2c, it can be seen that a certain amount of WO₃ is attached to the surface of self-assembled PDI supermolecule, and there are also very small Cu nanoparticles around it. According to the HRTEM image of WO₃ (Fig. 2d), the lattice parameter of WO₃ can be determined to be 0.377 nm, corresponding to its (0 2 0) plane [8]. It can also be noted that Cu NP (1 1 1) with a lattice parameter of 0.21 nm was supported on the WO₃. In addition, the EDX mapping element analysis is given in Fig. 2(e–j), which can confirm that the elements of the composites include C, O, N, Cu and W. From the mapping of the W and Cu elements, it can be seen that the distribution of Cu and W is the same, but Cu is less in content with respect to W, which is completely in line with the experimental results. These results show the tight connectivity of the components between the composites, which is beneficial for the photocatalytic process.

Figs. 3 and S3 show the XPS investigation of WO₃, WO₃@Cu and 30% WO₃@Cu@PDI. The binding energy of samples was corrected by C 1s binding energy 284.8 eV. As can be seen from Fig. 3a, the peak signals (C, N, O, W and Cu) are present. Compared with Fig. 3b, the peak intensity of W 4f and W 4d decreases greatly [9]. From the C 1s pattern of Fig. 3c, there are four peaks at 284.8 eV, 286.1 eV, 287.8 eV, and 289.2 eV, which can be considered as C=C, C–C/C–N, C=O bonds and π -excitation, respectively [26]. For N 1s pattern of Fig. 3d, only C–N bond exists in self-assembled PDI supermolecule, so there is only one peak signal at 400.08 eV. All of Fig. 3c and d show the existence of self-assembled PDI supermolecule. From the O 1s pattern of Fig. 3e, WO₃@Cu@PDI has three more peak signals than WO₃, which also shows the successful synthesis of the composites. From W 4f pattern of Figs. 3f and S3b, it can be seen that the peak widths of WO₃@Cu@PDI and WO₃@Cu become larger, but the height of the peak becomes lower compared with the W 4f pattern of WO₃ oxide. And it can be also seen that the binding energy of 30% WO₃@Cu@PDI can be reduced by 0.38 eV compared with the binding energy of the pristine WO₃. The binding energy of WO₃@Cu is reduced by 0.2 eV compared with the pristine WO₃. Since the binding energy is related to the charge density,

it can be seen from the results of this change that the amount of charge transfer on the WO₃ in the composite material is much higher. In addition, it can be seen from Cu 2p of Fig. S3c that the binding energy of WO₃@Cu can be reduced by 0.18 eV compared with 30% WO₃@Cu@PDI. Therefore, according to the result of W 4f and Cu 2p can well demonstrate the electron flow mechanism of the Z-scheme. The excited electrons on the WO₃ are transferred to the Cu and then to the PDI supramolecules (Scheme 2) [27].

The UV–vis diffuse reflectance spectra of PDI, WO₃ and 30% WO₃@Cu@PDI is given in Fig. 4a. It can be noted that WO₃ has a lower visible light response, only light with wavelength less than 470 nm can be absorbed. In the ultraviolet region, the absorption intensity of WO₃ is greater than composite. However, it is noteworthy that WO₃@Cu@PDI can absorb light with wavelength of 760 nm. Additionally, WO₃@Cu@PDI absorption intensity of visible light ($\lambda > 420$ nm) is higher than PDI. All these phenomena show that the light absorption of composite between pre-prepared samples is better. Here, the E_g values of various materials are determined by Kubelka-Munk method. As can be seen from Fig. 4b, the E_g values of WO₃ and self-assembly PDI supermolecule is 2.73 eV and 1.68 eV, respectively. The Mott-Schottky curve is used to measure the flat-band potential of materials, and the flat-band potential minus 0.2 eV is considered to be the conduction band of n-type semiconductors [28]. According to the intercept of tangent lines in the Fig. 4(c, d), the U_{fb} of WO₃ and self-assembled PDI supermolecules are 0.70 eV and –0.26 eV, respectively. Naturally, the conduction bands of WO₃ and self-assembled PDI supermolecules are 0.5 eV and –0.46 eV vs SCE. By conversion, we can further obtain that the CB of WO₃ and self-assembled PDI supermolecules are 0.74 eV and –0.22 eV vs NHE (Normal Hydrogen Electrode). From the values of E_g and CB of the semiconductor obtained above, it is easy to get the values of valence band, VB (WO₃) = 3.47 eV, VB (self-assembled PDI) = 1.46 eV.

The fluorescence data of self-assembled PDI supermolecules and 30% WO₃@Cu@PDI is given in Fig. S2 (the excitation wavelength is 468 nm). We can see that the fluorescence intensity of composites is lower, which means that the recombination rate of electronic-holes pairs in composites is greatly reduced. In photocatalytic reaction, the more separated electrons and holes, the more efficient the photocatalytic reaction is. Therefore, according to the fluorescence data, the photocatalytic active of the composites is improved.

The nitrogen (N₂) physisorption isotherms were measured and analyzed to characterize the textural properties of the samples (Table S1). The Barret–Joyner–Halenda (BJH) pore-size distribution curves are presented in the inset of Fig. S4. It can be found that WO₃, PDI and 30% WO₃@Cu@PDI are all unimodal pore size distribution. The Brunauer–Emmett–Teller (BET) specific surface area (S_{BET}) of PDI is 15.499 m²/g, which is larger than that of WO₃ (13.634 m²/g). After combining WO₃, Cu and PDI, 20% WO₃@Cu@PDI has a slight decrease

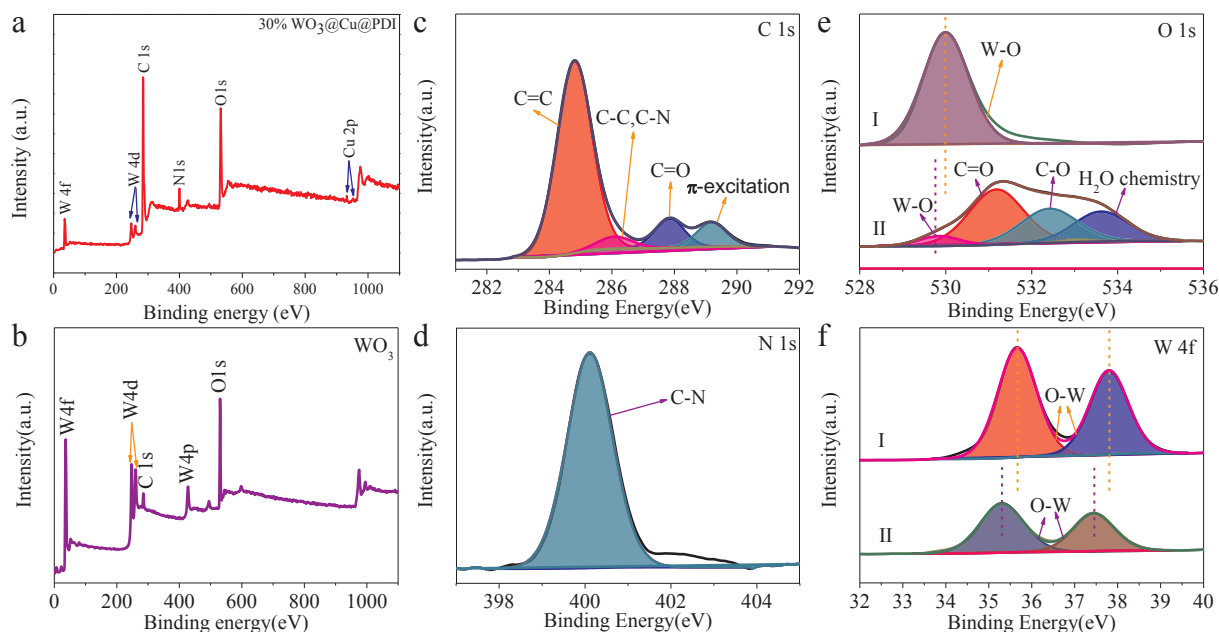


Fig. 3. (a) Survey XPS spectrum of $\text{WO}_3@Cu@PDI$ composite. (b) Survey XPS spectrum of WO_3 . High-resolution XPS spectrum of C 1s (c), N 1s (d) of $\text{WO}_3@Cu@PDI$ composite, High-resolution XPS spectrum of O 1s (e), W 4f (f) of (I) WO_3 and (II) $\text{WO}_3@Cu@PDI$ composite.

in the specific surface area, and the rest of the samples have increased, of which 30% $\text{WO}_3@Cu@PDI$ has increased by 1.4 times, which is beneficial to the reaction.

3.2. Improvement of photocatalytic activity of as-prepared samples

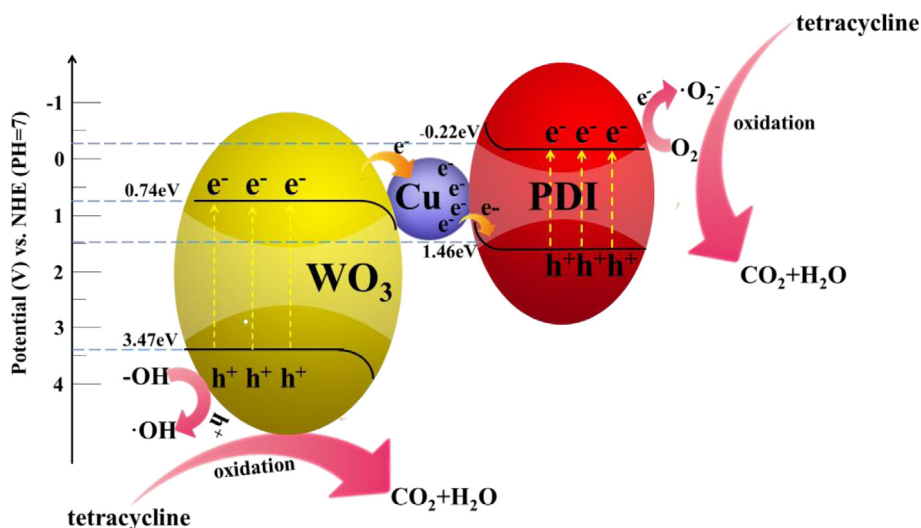
In Fig. 5a, under visible light ($\lambda > 420 \text{ nm}$), the degradation rate of TC by WO_3 , PDI (no self-assembly), PDI supermolecule (self-assembled) and $\text{WO}_3@Cu@PDI$ (20%, 30%, 40%) were compared. The reaction kinetics curves of the above materials are given in Fig. 5b. UV-Visible absorbance spectra of composites for degradation are given in Fig. S5. According to the kinetic constants of each material, the degradation rate of 30% $\text{WO}_3@Cu@PDI$ is five times higher than self-assemble PDI supermolecule and 40 times than sole WO_3 . The result is mainly due to the construction of Z-scheme system, which keeps the strong redox ability of WO_3 . At the same time, because of the existence of Z-scheme, the separation of photogenerated carriers is accelerated, resulting in more $=\text{O}_2^-$ and $\cdot\text{OH}^-$ generated in the reaction solution. Therefore,

the formation of Z-scheme contains advantages of retain redox ability and rapid transfer of photogenerated carriers, greatly improving the degradation efficiency of TC.

As can be seen from Fig. 5, the higher degradation efficiency was around 75%. Therefore, in order to better evaluate the activity of the composite, the experiment of prolonging the time and increasing the dose is shown in Fig. S6. When the amount of the catalyst is 5 mg, after two hours of operation, the degradation efficiency is very low, and the maximum degradation rate is about 10%. When the amount of catalyst is increased by 10 mg, the TC can be degraded in half an hour. Low doses of catalyst are not very sensitive to low concentrations of TC solution.

3.3. Influence of inorganic salts and testing of photocatalyst stability

In order to evaluate whether inorganic ions have an impact on photocatalytic performance, Fig. 6a shows photocatalytic degradation curve after adding inorganic ions. Here, in the degradation experiment,



Scheme 2. Z-scheme electron transfer mechanism.

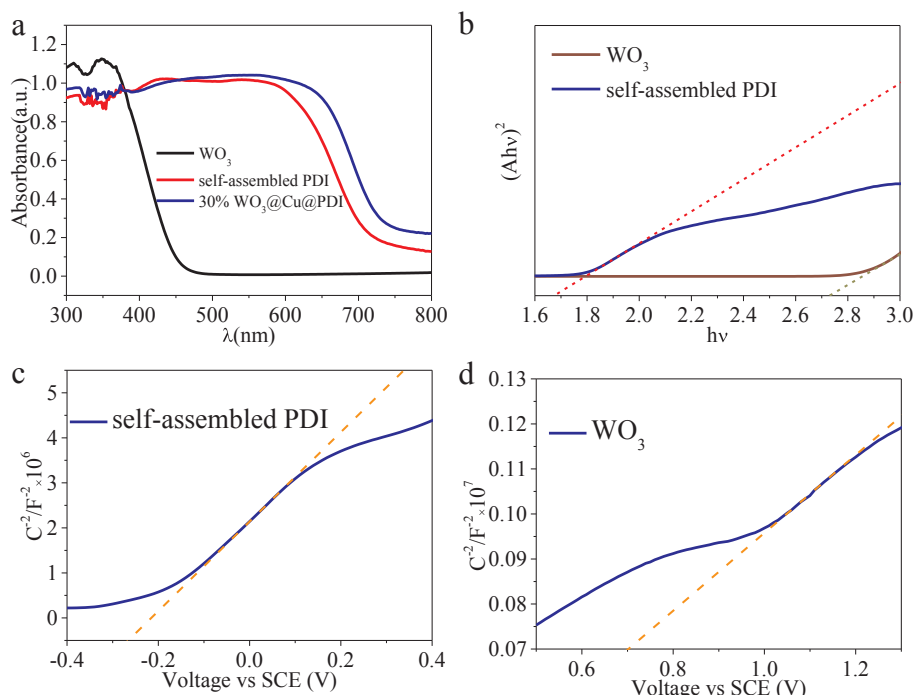


Fig. 4. (a) UV-vis diffuse reflectance spectra, (b) Kubelka-Munk curve of different samples, (c and d) the Mott-Schottky plot of different samples.

0.325 mmol of KCl and 0.12 mmol/L NaNO₃ solution was added to the TC solution. The results show that the degradation efficiency decreases with the addition of inorganic ions, but the change is negligible. Therefore, the presence of these four inorganic ions has no effect on the degradation of TC.

It is expected that the photocatalyst can maintain high photocatalytic activity after repeated use. According to repeated experimental curve of Fig. 6b, 30% WO₃@Cu@PDI maintains high activity after three runs. In addition, it can be seen that the degradation rate reduced by about 10% at the second run. By the third cycle, the degradation rate has stabilized, which may be due to the transfer of photogenerated electrons to the surface of composites over time [23,24]. Similarly, the XRD results before and after three cycles and the Cu 2p pattern results before and after three cycles are given in Fig. S7. It can be seen from Fig. S7a that the XRD peaks of the catalysts before and after the reaction are identical, indicating that the reaction does not change for the structure of the composite. The XPS detection results of Cu 2p (Fig. S7b) are also consistent, which shows that Cu is not oxidized. Therefore, it can be concluded that the catalyst is stable and can be effectively recycled.

3.4. Measurement of photoelectrochemical properties

Curves of photocurrent and electrochemical impedance spectroscopy (EIS) are given by Fig. 7. As shown in Fig. 7a, the composite has a largest photocurrent. Moreover, it can be seen that the photocurrent of 30% WO₃@Cu@PDI reaches 1.7 $\mu\text{A cm}^{-2}$, which is 1.7 times higher than WO₃ and 2.4 times than self-assembled PDI. Therefore, since the composite has highest separation efficiency of photogenerated carriers, it has strongest redox ability in photocatalytic process [6]. In addition, it can also be found that the photocurrent of 30% WO₃@Cu@PDI decreases with time, which may be due to the transfer of photogenerated electrons to the surface of composites over time. Fig. 7b shows the electrochemical impedance spectroscopy Nyquist plot of WO₃, self-assembled PDI supermolecule and 30% WO₃@Cu@PDI under light and dark conditions. As shown from Fig. 7b, the 30% WO₃@Cu@PDI has the minimum arc radius, indicating that more electron-hole pairs are separated, which is consistent with result of photocurrent curve [29]. At the same time, it can be seen that the arc radius of each material decreases to a certain extent after the illumination. Therefore, according to the photo-electrochemical properties of the samples tested, the same results can be obtained as the above fluorescence, UV-vis diffuse reflectance spectra, and degradation tests.

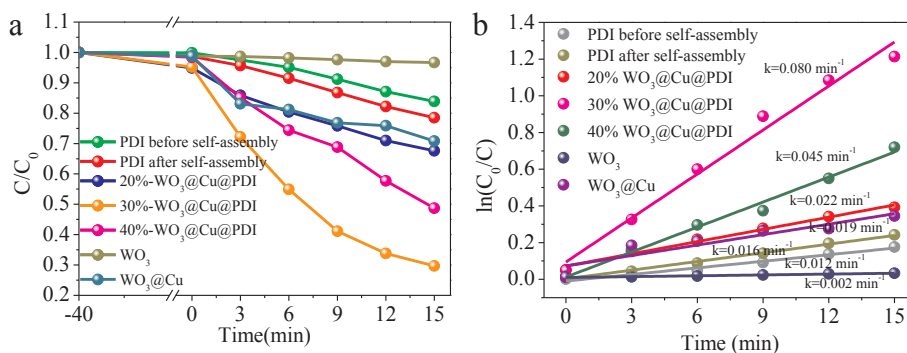


Fig. 5. (a) Photodegradation curves of as-prepared samples with different proportions under visible light ($\lambda > 420 \text{ nm}$) conditions; (b) reaction kinetics curves of samples.

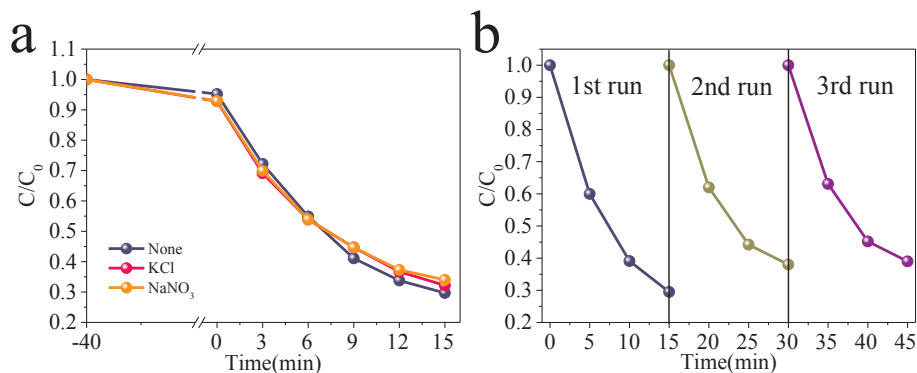


Fig. 6. (a) Photodegradation TC curves containing different inorganic salts. (b) Repeated photodegradation of sample of optimize mass ratio.

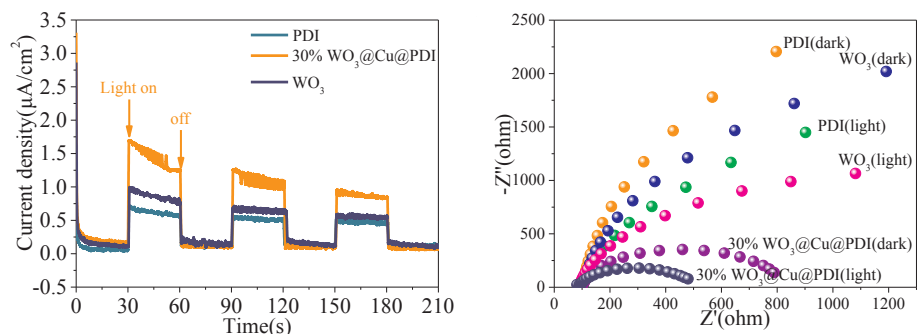
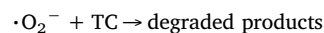
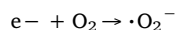
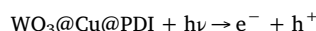


Fig. 7. (a) Transient photocurrent curve of as-prepared samples; (b) EIS Nyquist plots of as-prepared samples under illumination and darkness.

3.5. Electron transfer mechanism of Z-scheme

Herein, in order to prove the electron transfer of $\text{WO}_3\text{@Cu@PDI}$, an indirect method was adopted, which was achieved by detecting the positions of superoxide radicals ($\cdot\text{O}_2^-$), hydroxyl radicals ($\cdot\text{OH}$) and h^+ in the composite. Therefore, benzoquinone (BQ), ethylenediaminetetraacetate (EDTA), Isopropanol (IPA) and AgNO_3 were selected as scavengers for $\cdot\text{O}_2^-$, h^+ , $\cdot\text{OH}$, e^- , respectively. TC as a target pollutant was used to evaluate the effects of sacrificial agents in the reaction. As can be seen from Fig. 8a, the addition of IPA has only slightly changed compared with the reaction without sacrificial agent, which indicates that $\cdot\text{OH}^-$ is not the main active species in the reaction. At the same time, it can also be noted that the degradation rate increases with the addition of AgNO_3 , which indicates that e^- are not the main active species. And the increase of the degradation rate may be due to the Ag deposited on the catalyst, which accelerates the separation rate of photogenerated carriers and thus accelerates the degradation rate. However, when BQ and EDTA are added, the degradation rate is greatly reduced, indicating that the active species of $\text{WO}_3\text{@Cu@PDI}$ composite in the degradation of TC are mainly h^+ and $\cdot\text{O}_2^-$. Because of the location of WO_3 conduction band, WO_3 does not produce $\cdot\text{O}_2^-$. Namely, $\text{WO}_3\text{@Cu}$ can't produce active radicals $\cdot\text{O}_2^-$. To further prove the correctness of the above sacrificial experiment, the ESR results are given in Fig. 8(b–e). Fig. 8b and c give ESR response peak curves of $\text{DMPO}\cdot\text{OH}^-$ and $\text{DMPO}\cdot\text{O}_2^-$ of 30% $\text{WO}_3\text{@Cu@PDI}$, respectively. Under visible light irradiation, $\text{DMPO}\cdot\text{OH}^-$ and $\text{DMPO}\cdot\text{O}_2^-$ of 30% $\text{WO}_3\text{@Cu@PDI}$ have four peak signals, and the intensity of this peak signal increases with time. However, in the dark environment, there is no peak signal. The results of ESR detection show that because of the existence of Z-scheme, $\cdot\text{O}_2^-$ and $\cdot\text{OH}^-$ can be generated in the $\text{WO}_3\text{@Cu@PDI}$, which are consistent with sacrificial experiments. In order to prove the $\cdot\text{O}_2^-$ are produced from the self-assembled PDI molecule. The ESR results of the self-assembled PDI molecule are given from Fig. 8(d–e). According to the results of Fig. 8(d–e), it can be proved that self-assembled PDI molecule can produce $\cdot\text{O}_2^-$ and $\cdot\text{OH}^-$

under the irradiation of visible light. Based on the above sacrificial experiments and ESR results, we can deduce that the possible reactions are as follows:



Based on the above conclusions, we can preliminarily determine the electron transfer path between WO_3 and self-assembled PDI molecule. As Scheme 2 shows that the photogenerated electrons on WO_3 conduction band pass through the copper intermediate to the valence band of self-assembled PDI molecule, and the transferred electrons recombine with the photogenerated holes in time. Electrons on conduction band of self-assembled PDI molecule generate $\cdot\text{O}_2^-$ by reducing O_2 , which explains why $\cdot\text{O}_2^-$ are the main active species in the reaction process. In order to make this scheme more convincing, the comparison of XPS binding energy between WO_3 and $\text{WO}_3\text{@Cu@PDI}$ is also given here. The binding energy is related to the electronic density of materials, and the surface electron density of the material decreases as the binding energy decreases [27]. As can be seen from Figs. 3(e, f) and S3(b, c), the binding energy of W-O of $\text{WO}_3\text{@Cu}$ decreases, which indicate that the electronic density on the surface of Cu increases, thus explain the transformation of electrons WO_3 to Cu. Similarly, in the pattern of Cu 2p, the binding energy of $\text{WO}_3\text{@Cu@PDI}$ is lower than that of $\text{WO}_3\text{@Cu}$, indicating that the electrons on the Cu are then transferred to the PDI supramolecules. Therefore, the results of XPS are also a good demonstration of the mechanism of electron transport.

3.6. A potential degradation pathway of TC

In order to understand the degradation pathway and mechanism of composite, the degradation intermediates of TC over $\text{WO}_3\text{@Cu@PDI}$

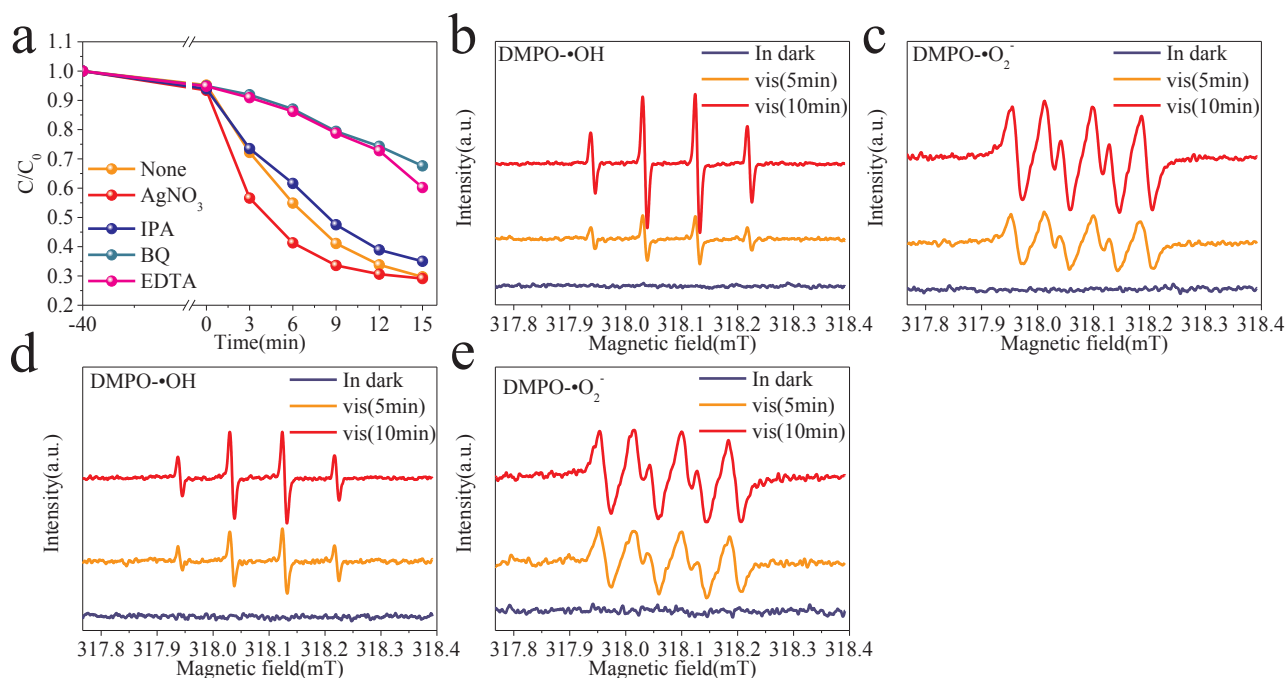


Fig. 8. (a) Photodegradation curves of TC with additions of scavengers under visible light, (b) Spin-trapping ESR spectra of DMPO·OH over WO₃@Cu@PDI in aqueous dispersions, (c) Spin-trapping ESR spectra of DMPO·O₂⁻ over WO₃@Cu@PDI in methanol dispersions; (d) Spin-trapping ESR spectra of DMPO·OH over PDI in aqueous dispersions, (e) Spin-trapping ESR spectra of DMPO·O₂⁻ over PDI in methanol dispersions.

were identified by LC-MS/MS (Fig. S8). According to the emerged intermediate products and the previous reports, a potential TC degradation pathway was proposed (Fig. S9). The degradation process of TC includes deacylation; hydroxylation; the elimination of amide group; carboxyl; ketone group; *N*-demethylation; substitution ring-opening reaction and mineralization. After this series of reactions, the TC is finally mineralized into CO₂ and H₂O.

4. Conclusion

In this work, WO₃@Cu@PDI Z-scheme was synthesized by two steps. First, copper was deposited on WO₃ by a method of photo-deposition, and then WO₃@Cu@PDI was synthesized by a water bath method. The synthesized materials had very high photocatalytic activity under visible light. Under visible light irradiation, the degradation rate of composites is 40 times faster than that of sole WO₃ and 5 times than PDI. The photocatalytic activity of WO₃@Cu@PDI toward TC still kept 85% after three reuses. The presence of Cl⁻, Na⁺, K⁺, NO₃⁻ had no effect on the activity of the catalyst. Z-scheme enabled the photogenerated electrons on WO₃ to quickly transfer to the donor level of self-assembled PDI molecule and recombined with h⁺ in time to make e⁻ on CB of self-assembled PDI supermolecule and h⁺ on VB of WO₃ accumulated more and had stronger redox active.

Acknowledgements

This work was supported by the National Natural Science Foundation of China (51672077, 51872089), Hunan Provincial Natural Science Foundation of China (2017JJ2026), Key Laboratory of Jiangxi Province for Persistent Pollutants Control and resources Recycle (Nanchang hangkong University) (ES201880051).

Appendix A. Supplementary data

Supplementary data to this article can be found online at <https://doi.org/10.1016/j.cej.2019.122691>.

References

- [1] J. Luo, T. Liu, D. Zhang, K. Yin, D. Wang, W. Zhang, C. Liu, C. Yang, Y. Wei, L. Wang, S. Luo, J.C. Crittenden, The individual and Co-exposure degradation of benzophenone derivatives by UV/H₂O₂ and UV/PDS in different water matrices, *Water Res.* 159 (2019) 102–110.
- [2] L. Wang, X. Liu, J. Luo, X. Duan, J. Crittenden, C. Liu, S. Zhang, Y. Pei, Y. Zeng, X. Duan, Self-optimization of the active site of molybdenum disulfide by an irreversible phase transition during photocatalytic hydrogen evolution, *Angew. Chem. Int. Ed.* 56 (2017) 7610–7614.
- [3] S. Zhang, X. Liu, C. Liu, S. Luo, L. Wang, T. Cai, Y. Zeng, J. Yuan, W. Dong, Y. Pei, Y. Liu, MoS₂ quantum dot growth induced by S vacancies in a ZnIn₂S₄ monolayer: atomic-level heterostructure for photocatalytic hydrogen production, *ACS Nano* 12 (2018) 751–758.
- [4] S.L. Wang, Y. Zhu, X. Luo, Y. Huang, J. Chai, T.I. Wong, G.Q. Xu, 2D WC/WO₃ heterogeneous hybrid for photocatalytic decomposition of organic compounds with vis-NIR light, *Adv. Funct. Mater.* 28 (2018).
- [5] O. Tomita, T. Otsubo, M. Higashi, B. Ohtani, R. Abe, Partial oxidation of alcohols on visible-light-responsive WO₃ photocatalysts loaded with palladium oxide cocatalyst, *ACS Catal.* 6 (2016) 1134–1144.
- [6] H. Chen, Y. Liu, T. Cai, W. Dong, L. Tang, X. Xia, L. Wang, T. Li, Boosting photocatalytic performance in mixed-valence MIL-53(Fe) by changing FeII/FeIII ratio, *ACS Appl. Mater. Interfaces* 11 (2019) 28791–28800.
- [7] T. Hu, P. Li, J. Zhang, C. Liang, K. Dai, Highly efficient direct Z-scheme WO₃/CdS-diethylenetriamine photocatalyst and its enhanced photocatalytic H₂ evolution under visible light irradiation, *Appl. Surf. Sci.* 442 (2018) 20–29.
- [8] L. Jiang, X. Yuan, G. Zeng, J. Liang, X. Chen, H. Yu, H. Wang, Z. Wu, J. Zhang, T. Xiong, In-situ synthesis of direct solid-state dual Z-scheme WO₃/g-C₃N₄/Bi₂O₃ photocatalyst for the degradation of refractory pollutant, *Appl. Catal. B: Environ.* 227 (2018) 376–385.
- [9] W. Yu, J. Chen, T. Shang, L. Chen, L. Gu, T. Peng, Direct Z-scheme g-C₃N₄/WO₃ photocatalyst with atomically defined junction for H₂ production, *Appl. Catal. B: Environ.* 219 (2017) 693–704.
- [10] J. Zhang, H. Ma, Z. Liu, Highly efficient photocatalyst based on all oxides WO₃/Cu₂O heterojunction for photoelectrochemical water splitting, *Appl. Catal. B: Environ.* 201 (2017) 84–91.
- [11] I. Grigioni, K.G. Stamplecoskie, E. Selli, P.V. Kamat, Dynamics of photogenerated charge carriers in WO₃/BiVO₄ heterojunction photoanodes, *J. Phys. Chem. C* 119 (2015) 20792–20800.
- [12] J.H. Baek, B.J. Kim, G.S. Han, S.W. Hwang, D.R. Kim, I.S. Cho, H.S. Jung, BiVO₄/WO₃/SnO₂ double-heterojunction photoanode with enhanced charge separation and visible-transparency for bias-free solar water-splitting with a perovskite solar cell, *ACS Appl. Mater. Interfaces* 9 (2017) 1479–1487.
- [13] P. Zhou, J. Yu, M. Jaroniec, All-solid-state Z-scheme photocatalytic systems, *Adv. Mater.* 26 (2014) 4920–4935.
- [14] Y. Jia, S. Li, J. Gao, G. Zhu, F. Zhang, X. Shi, Y. Huang, C. Liu, Highly efficient (BiO)₂CO₃-BiO_{2-x}-graphene photocatalysts: Z-scheme photocatalytic mechanism for

- their enhanced photocatalytic removal of NO, *Appl. Catal. B: Environ.* 240 (2019) 241–252.
- [15] Y. Yang, Z. Zeng, C. Zhang, D. Huang, G. Zeng, R. Xiao, C. Lai, C. Zhou, H. Guo, W. Xue, M. Cheng, W. Wang, J. Wang, Construction of iodine vacancy-rich BiOI/Ag@AgI Z-scheme heterojunction photocatalysts for visible-light-driven tetracycline degradation: transformation pathways and mechanism insight, *Chem. Eng. J.* 349 (2018) 808–821.
- [16] H. Zhou, Z. Wen, J. Liu, J. Ke, X. Duan, S. Wang, Z-scheme plasmonic Ag decorated WO₃/Bi₂WO₆ hybrids for enhanced photocatalytic abatement of chlorinated-VOCs under solar light irradiation, *Appl. Catal. B: Environ.* 242 (2019) 76–84.
- [17] X. Yuan, L. Jiang, X. Chen, L. Leng, H. Wang, Z. Wu, T. Xiong, J. Liang, G. Zeng, Highly efficient visible-light-induced photoactivity of Z-scheme Ag₂CO₃/Ag/WO₃ photocatalysts for organic pollutant degradation, *Environ. Sci. Nano* 4 (2017) 2175–2185.
- [18] Z. Li, J. Lyu, K. Sun, M. Ge, Construction of magnetic AgBr/Cu/CuFe₂O₄ Z-scheme photocatalyst with improved photocatalytic performance, *Mater. Lett.* 214 (2018) 257–260.
- [19] S. Patnaik, G. Swain, K.M. Parida, Highly efficient charge transfer through a double Z-scheme mechanism by a Cu-promoted MoO₃/g-C₃N₄ hybrid nanocomposite with superior electrochemical and photocatalytic performance, *Nanoscale* 10 (2018) 5950–5964.
- [20] R. Kuriki, H. Matsunaga, T. Nakashima, K. Wada, A. Yamakata, O. Ishitani, K. Maeda, Nature-inspired, highly durable CO₂ Reduction system consisting of a binuclear ruthenium(II) complex and an organic semiconductor using visible light, *J. Am. Chem. Soc.* 138 (2016) 5159–5170.
- [21] K. Sekizawa, K. Maeda, K. Domen, K. Koike, O. Ishitani, Artificial Z-scheme constructed with a supramolecular metal complex and semiconductor for the photocatalytic reduction of CO₂, *J. Am. Chem. Soc.* 135 (2013) 4596–4599.
- [22] D. Liu, J. Wang, X. Bai, R. Zong, Y. Zhu, Self-assembled PDINH supramolecular system for photocatalysis under visible light, *Adv. Mater.* 28 (2016) 7284–+.
- [23] J. Wang, W. Shi, D. Liu, Z. Zhang, Y. Zhu, D. Wang, Supramolecular organic nanofibers with highly efficient and stable visible light photooxidation performance, *Appl. Catal. B: Environ.* 202 (2017) 289–297.
- [24] T. Cai, Y. Liu, L. Wang, S. Zhang, J. Ma, W. Dong, Y. Zeng, J. Yuan, C. Liu, S. Luo, Dark deposition of Ag nanoparticles on TiO₂: improvement of electron storage capacity to boost memory catalysis activity, *ACS Appl. Mater. Interfaces* 10 (2018) 25350–25359.
- [25] K. Zhang, J. Wang, W. Jiang, W. Yao, H. Yang, Y. Zhu, Self-assembled perylene diimide based supramolecular heterojunction with Bi₂WO₆ for efficient visible-light-driven photocatalysis, *Appl. Catal. B: Environ.* 232 (2018) 175–181.
- [26] H. Miao, J. Yang, Y. Wei, W. Li, Y. Zhu, Visible-light photocatalysis of PDI nanowires enhanced by plasmonic effect of the gold nanoparticles, *Appl. Catal. B: Environ.* 239 (2018) 61–67.
- [27] T. Cai, L. Wang, Y. Liu, S. Zhang, W. Dong, H. Chen, X. Yi, J. Yuan, X. Xia, C. Liu, S. Luo, Ag₃PO₄/Ti₃C₂ MXene interface materials as a Schottky catalyst with enhanced photocatalytic activities and anti-photocorrosion performance, *Appl. Catal. B: Environ.* 239 (2018) 545–554.
- [28] Y. Matsumoto, Energy positions of oxide semiconductors and photocatalysis with iron complex oxides, *J. Solid State Chem.* 126 (1996) 227–234.
- [29] Y. Zhu, L. Wang, Y. Liu, L. Shao, X. Xia, In-situ hydrogenation engineering of ZnIn₂S₄ for promoted visible-light water splitting, *Appl. Catal. B: Environ.* 241 (2019) 483–490.